SAND2011-4467C

SIMULATIONS OF DYNAMIC LASER / PLASMA X-RAY PRODUCTION *

D. R. Welch, C. L. Miller+, D. V. Rose
Voss Scientific, LLC, 418 Washington Street, SE
Albuquerque, New Mexico 87108 USA

R. B. Campbell, B. V. Oliver, T. J. Webb, D. G. Flicker
Sandia National Laboratories
Albuquerque, New Mexico 87185-1195 USA

Abstract

A high fluence X-ray diagnostic is being developed by Sandia National Laboratories for use as a point-projection X-ray source for imaging high-density load dynamics on the ZR pulsed power facility. The LSP 3D PIC code was used to model the dynamic interaction, between the Z-Petawatt IR laser and a high-atomic-number thin foil, which generates the intense short-duration bremsstrahlung X-ray pulse. Particle kinematics are explicit for densities near and below critical and implicit for higher densities through solid. Sufficiently small cell-sizes and timesteps were used to fully resolve the laser-plasma interaction and subsequent electron dynamics in the foil -- 15 million cells and 400 million particles were required. An optional treatment of high-energy electrons as non-interacting test particles was also examined. The particle-field solution used matrix inversion techniques as opposed to a conventional ADI scheme. The effect of parameters such as foil radius, tilt angle, foil support structure, and net laser energy on the X-ray fluence and energy spectrum were evaluated in both cylindrical and 3D Cartesian coordinates for all angle leaving the target. The simulated X-ray fluence produced a peak X-ray dose in excess of 200 mRad, consistent with experimental measurements.

I. INTRODUCTION

Energy, Stockpile Surety, and National Security missions require probing matter of ever increasing density at higher resolutions, necessitating higher energy X-ray sources [1]. Sandia National Laboratories is pursuing a project to create a new point-projection diagnostic for imaging dense objects produced on Z utilizing bremsstrahlung radiography with the X-rays generated by the Z-Petawatt [2] laser / high-atomic-number converter interactions. There has been successful work at Sandia in producing K-alpha sources with the Beamlet [3,4] laser, and imaging Z-relevant objects using both point projection methods as well as bent crystal imaging. However, these sources are limited to energies below 40 keV, which may not be adequate to image the denser samples of future interest. On the other hand, workers at the Vulcan laser facility have demonstrated PW laser / foil bremsstrahlung sources at very high fluence and energy for ultrahigh density applications [5,6].

Here, LSP [7] is used to simulate such dynamic interactions between intense IR lasers striking high-atomic-number foils [8]. The calculations combine both the laser / plasma interaction (LPI) near the critical surface and the subsequent high-energy electron dynamics and bremsstrahlung production into a fully-integrated 3D simulation model of the entire foil, using both cylindrical and Cartesian coordinates. Many details of the LPI simulation model have been discussed previously, and will be summarized in Section II. In Section III, a series of 3D cylindrical simulations are presented to characterize the dose production as a function of foil radius. In Section IV, 2D Cartesian simulations results are presented. In Section V, 3D Cartesian simulation models and results are presented. Cartesian simulations provide improved resolution of the tilted foils but at a significantly higher computational cost. A summary of the significant findings of this work is given in Section VI.

II. SIMULATION MODEL

The picosecond-scale, IR laser pulse strikes a dense thin-foil gold target, where the high field intensity accelerates electrons to high energies. These electrons propagate through the dense gold plasma, where the electron-ion interaction produces bremsstrahlung X-rays, which are then transported to the edges of the simulation space. Once an X-ray macroparticle reaches the edge of the simulation space, ensuring its interaction with the target was over, the x-, y-, and z-components of its momentum and location, along with the time and

* Work supported by Sandia National Laboratories. Sandia National Laboratories is a multi-program laboratory operated by Sandia Corporation, a wholly owned subsidiary of Lockheed Martin Company, for the United States Department of Energy's National Nuclear Security Administration under contract DE-AC04-94-AL85000.
+ e-mail: craigm@vosssci.com

macroparticle weight are saved to a particle extraction file. These particle extraction files, one for each boundary face, can be used as inputs for a simple transport simulation that carry the particles to a spherical target with a 1 meter radius. Here, the X-ray number fluences are scaled by a factor of 2.6×10^{-10} (characteristic of a several-MV diode source) to get a reasonable estimate of the dose -- a strictly accurate dose calculation would depend on the detailed energy spectrum of the X-rays and the specific detector.

The gold foil is modeled as a volume of doubly-ionized gold ions with 6×10^{22} cm^{-3} number density overlapped by electrons with a twice this number density (1.2×10^{23} cm^{-3}). This ensures charge neutrality at the start of the simulations. Typical length scales were 100 μm for the target disk diameter and 10 μm for its thickness; a 100 μm by 100 μm square foil was also used. A nominally 20 μm thick, exponentially-decaying density (3 μm characteristic length) plasma was included in front of the foil to simulate blow off from the laser pre-pulse. A diagram of the generalized geometry is shown in Figure 1.

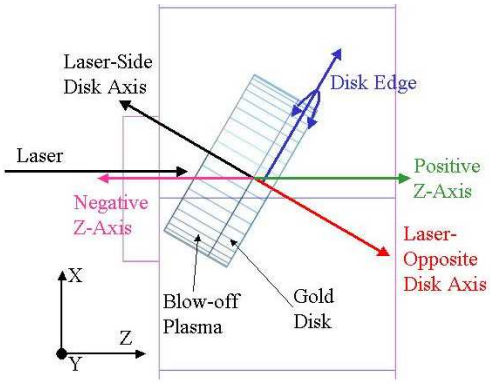

Figure 1. Typical simulation geometry. See also Section V.

The simulations used an energy-conserving, direct-implicit particle-in-cell (PIC) algorithm for particle kinematics [7]. This algorithm does not require Debye length spatial resolution and relaxes the need to resolve both the cyclotron and plasma frequencies. At low energies, electron collisions are modeled using Monte Carlo methods with cross-sections defined by Spitzer collisions. The electromagnetic field solution used an implicit solver with matrix inversion [9] using the PETSc linear algebra libraries [10].

Bremsstrahlung production in the gold foil is modeled using the Integrated Tiger Series [11] electron/photon transport algorithms, which have been integrated into LSP [12]. Photon energies and angles are tabulated at the point of generation and written to a file for post-processing.

III. DOSE DEPENDENCE ON FOIL RADIUS

For the initial simulations, a 3D cylindrical geometry was used with a circularly-polarized incident laser pulse delivering 75 J onto a 10 μm thick gold target using a square pulse with 20 fs rise- and fall-times and a 1.4 ps full width at half-maximum (FWHM). Figure 2 shows two plots of the number density of gold ions in a 3D cylindrical simulation of the 50 μm radius foil, before and after the laser pulse. The main part of the gold foil is colored red, while the blow-off plasma extends in front of the foil, towards the laser aperture. The laser pulse significantly bores through this blow-off plasma, but does not greatly affect the peak density regions. For these simulations, the only particle extraction was at the right hand side plane (+z), so these are the only X-rays available for the transport calculation. The normalized energy spectra from all three foils are plotted in Figure 3, and show very little variation with radius, especially at higher energies. Because of the logarithmic energy scale, the distribution data are normalized to the bin size so that the plot is normalized number per energy. The peak values are near 70 keV, while most of the photons have energies between 10 and 100 keV.

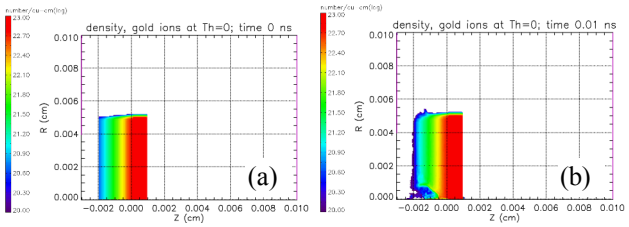

Figure 2. Number density plots of the 10 μm thick gold foil (a) before and (b) after illumination by the laser. The divot created by the energy deposition is clearly visible in the second image.

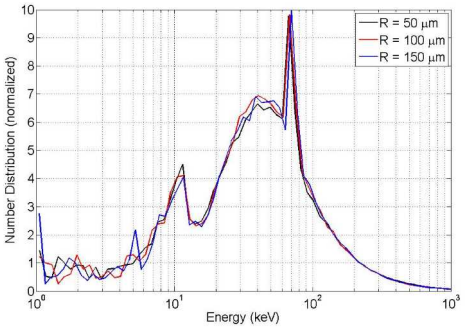

Figure 3. Photon energy spectrum for the three 10 μm thick gold foils of different radii, plotted from 1 keV to 1 MeV. Because of the logarithmic energy scale, the distribution data are normalized to the bin size so that the plot is normalized number per energy

The X-ray dose (from fluence scaling) plotted on a 1 meter sphere centered on the foil for 50 μm, 100 μm, and 150 μm radius foils are shown in Figure 4. In all cases, the dose shows significant variation due to the large number of sampling bins near the axis. These plots show a decreasing X-ray fluence with increasing target radius. The larger foils have larger capacitance and consequently a slower increase in the potential that inhibits further electrons from leaving the foil. The smaller foils, with a more rapid potential increase, will trap electrons at earlier times, confining more of them to the foil where the reflex

and generate X-rays. Thus, the larger foils confine less of the energy to create bremsstrahlung, resulting in a lower dose.

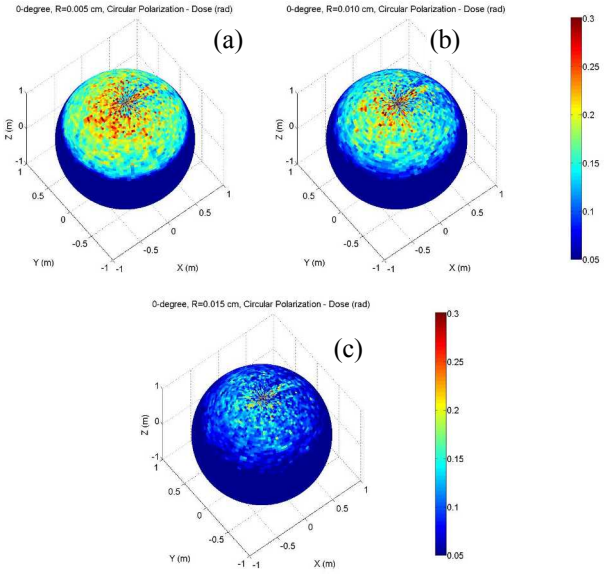

Figure 4. X-ray dose from scaled fluence at 1 meter after 10 ps for the 10 μm thick gold foils. The doses show significant variation due to the large number of sampling bins near the axis. Average dose values are: (a) 150-250 mRad for the 50 μm radius foil; (b) 130-220 mRad for the 100 μm radius foil; and (c) 100-200 mRad for the 150 μm radius foil.

IV. 2D CARTESIAN SIMULATIONS

The coarsely resolved (in θ) 3D cylindrical simulation geometry used above was found to be incompatible with a tilted gold foil. While very large 3D Cartesian simulations were a viable alternative, to speed the calculations the geometry was first changed to 2D Cartesian and the laser polarization changed to linear in the x-direction (P-Polarization). Because of this, the simulations quantities are recognized as being "per centimeter," which is the depth in the virtual y-direction. The 50 μm radius, 0º rotation result shows an averaged dose value nearly 50% greater than that of the corresponding cylindrical simulation (Figure 4). This difference is likely due to the lack of geometric fall off in Cartesian geometry and, possibly, the use of linear instead of circular polarization. The peak and averaged fluences, and average dose results for 10º, 20º, and 30º rotations of the foil summarized in Table 1. This data suggests the fluence depends on the foil angle, but not strongly. The weak dependence is likely the result of the blow-off plasma, which obscures the tilting.

Table 1. Summary of results for the rotated, 2D Cartesian gold foils.

Tilt Angle	Peak X-ray Fluence (#/cm)	Average X-ray Fluence (#/cm)	Average Dose (mRad)
0º	2.04×10^{9}	1.06×10^{9}	275.6
10º	3.28×10^{9}	1.32×10^{9}	343.2
20º	2.76×10^{9}	1.13×10^{9}	293.8
30º	4.57×10^{9}	1.38×10^{9}	358.8

V. 3D CARTESIAN SIMULATIONS

While the 2D Cartesian simulations were useful in examining trends affecting dose production, to get absolute results with a tilted foil, 3D Cartesian simulations were needed.

In order to resolve the 1 μm laser wavelength between the inlet boundary and gold target, an initial cell size of 0.125 μm (8 cells per wavelength) in the z-direction was needed. To minimize stress on the field solver from cells with large aspect ratios, the x- and y-dimensions of cells were limited to a factor of 4 larger the z-dimension. Away from the axis or behind the disk in the positive z-direction, the cell size limitations could be relaxed, though the linear sizes could not vary significantly from cell-to-cell (typically < 20%). The end result is a typical simulation space extending from +/- 100 μm (162 cells) in the x- and y-directions and from -30 μm to 100 μm (568 cells) in the z-direction, for just under 15 million cells. This is sufficient volume to enclose a 50 μm radius, tilted disk without it impinging upon the simulation boundary.

A typical value of 100 particles per cell of each species was chosen, in order to improve the energy conservation over that of the 3D cylindrical simulations. At the simulation start, there are only two species present, the low-energy electrons and the doubly-ionized gold ions. However, the fine grid resolution described above extends across much of the disk volume, requiring nearly 400 million particles per simulation. This could be relaxed somewhat with a thinner disk or blow-off plasma, but not significantly. The high particle count implies the simulation speed will be constrained by the particle kinematics, so an even distribution of particles across the utilized processors is the key to avoiding lengthy simulation times. Because of the size of the simulation, nearing the maximum of what the computing platform could handle, automatic domain rebalancing was unavailable for the initial simulations. A manual region and domain decomposition scheme was developed as an alternative.

The decomposition scheme partitioned the simulation space into 8 regions, monolithic in z, containing roughly the same number of particles. Regions with a larger number of cells are given slightly fewer particles to account for the larger field solve required. The z-direction decomposition is handled in a similar manner, by attempting to divide each region into a number of domains containing roughly the same number of particles.

Again, an attempt is made to put fewer particles into domains with a larger number of cells, as recognition of the more intensive field solve required there. The normalized cumulative particle count going from small z values to high ones shows that most of the particles lie between -20 μm and 40 μm, so the divisions should be the finest here. This division is made relatively general so it would be effective in all 8 domains, though the same approach can be used on each region individually. This scheme was found to provide a factor-of-two speed-up over a uniform distribution of domains within a region

The initial simulation densities of the gold ions and electrons are shown in Figure 5. As opposed to a true rotation about a central point, the particle distribution is defined by a tilt to the desired angle. This is not only easier to accomplish within LSP, but only differs from a true rotation near the disk edges, which should have a negligible effect on the simulation and resultant dose. Figure 6 shows similar density plots at 10 ps into a simulation using a 1.4 ps laser pulse delivering 130 J of field energy. The laser has partially penetrated the foil in filaments on the front face, though there is an ejection of particles from the front and rear faces.

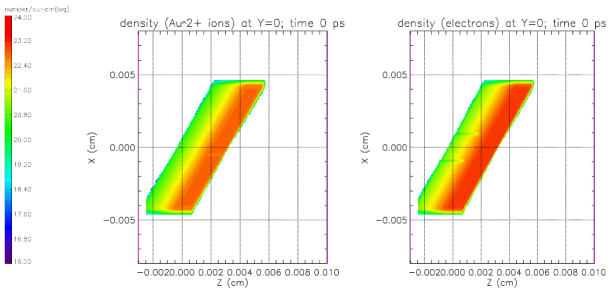

Figure 5. Cross-section plot from the P-polarized simulation at y = 0 of initial number density for: doubly ionized gold ions (left) and electrons (right).

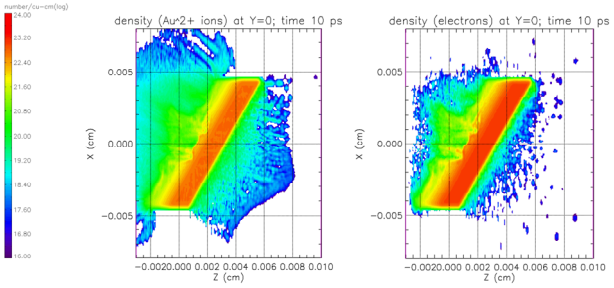

Figure 6. Cross-section plot from the P-polarized simulation at y = 0 and t = 10 ps of number density for: doubly ionized gold ions (left) and electrons (right).

The first two 3D Cartesian simulation runs examined the difference between S-Polarization, where the incident electric field is entirely tangential to the surface of the foil, and the P-Polarization, where the electric field has a component perpendicular to the surface. Both cases used a 30º tilt on a 50 μm radius foil, as in Figure 5, and used the same incident laser parameters: a 1.4 ps pulse length with a FWHM spot of 13.6 μm and total incident field energy of 130 J. Both simulations were run out to 10 ps with all X-rays leaving the system captured for the dose calculations. Time histories of the global X-ray count and energy, average energy per X-ray, and global electron kinetic energy are shown in Figure 7 and Figure 8. Both simulations showed similar rises and falls in all four categories, with the P-Polarization 10-15% higher in each case including integrated X-ray production. The P-Polarization simulation produced 8.66×10^{13} X-rays as compared to 7.78×10^{13} from the S-Polarization. Averaged over a 1 meter sphere and using the simple scaling from X-ray fluence to dose of 2.6×10^{-10}, P-Polarization produced a dose of 179.2 mRad, while the S-Polarization produced 161.0 mRad.

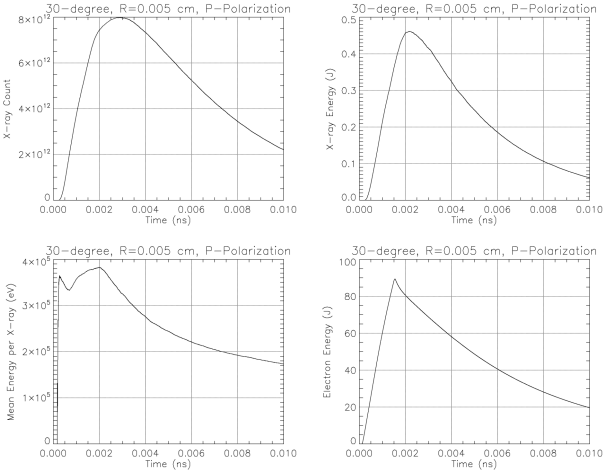

Figure 7. Time histories of global X-ray count, total X-ray energy, and energy per X-ray for the 3D Cartesian P-Polarization simulation.

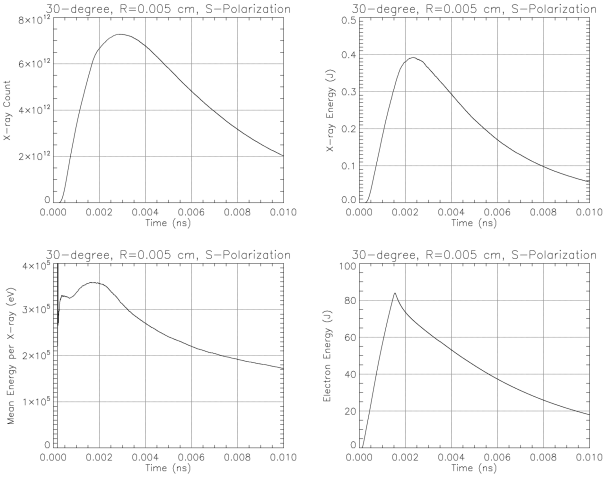

Figure 8. Time histories of global X-ray count, total X-ray energy, and energy per X-ray for the 3D Cartesian S-Polarization simulation.

The energy spectra (in number per keV) for the two simulations are plotted in Figure 9. The shapes of the two curves are essentially identical, with the P-Polarization curve uniformly 10% higher than the S-Polarization curve. This demonstrates that the difference between the two simulations is only in the energy deposition

efficiency of the laser pulse, with the subsequent electron and X-ray dynamics unchanged. Note that there is a significant photon component at higher energies (greater than ~200 keV) in both simulations.

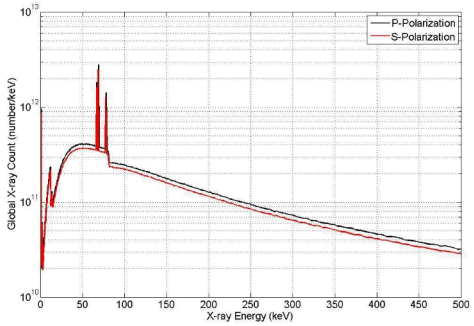

Figure 9. Global X-ray spectra for the two polarizations. The difference arises from the higher X-ray count for the P-polarization case. The normalization of both curves is identical for absolute comparison.

The angle-dependent doses are plotted in Figure 10, using the fluence-to-dose scaling from above and including particle extractions from all six sides of the simulation. Here, the doses show variation from ~140 mRad to ~230 mRad for P-Polarization and ~120 mRad to ~210 mRad for the S-Polarization. Unlike the 2D Cartesian simulations, which do not properly consider the transverse geometric fall off, these dose values are similar to the results of the 3D cylindrical simulations. Differences of ~10% between the cylindrical and Cartesian simulations can be attributed to the use of linear vs. circular polarization in the laser; the coarse azimuthal griding and lower particle numbers in the 3D cylindrical simulations; or worse statistics due to the lower number of X-rays produced in the cylindrical simulations.

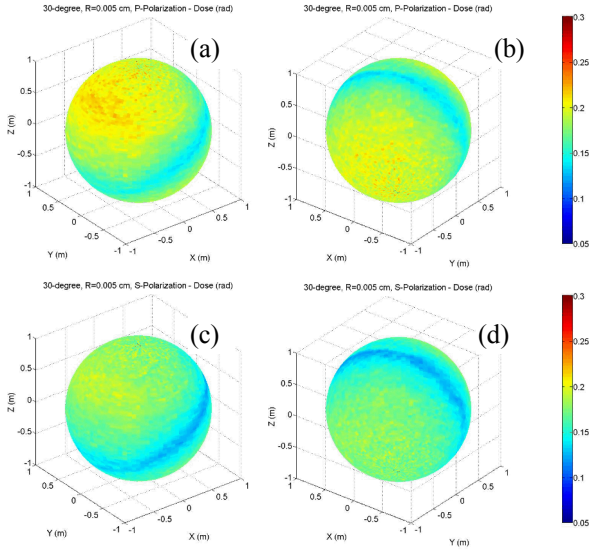

Figure 10. Target doses at 1 meter plotted onto spheres. Plots (a) and (b) are two views from opposite sides of the sphere for the P-Polarization case; (c) and (d) are the same views for the S-Polarization.

Lowering the incident energy of the laser pulse from ~130 J to ~90 J results in the dose distribution in Figure 11; here, only X-rays from the boundary at positive Z were saved and transported. The dose levels near the z-axis are ~130 mRad to ~150 mRad for the P-Polarization and ~120 mRad to ~140 mRad for the S-Polarization. The roughly 10% difference between the polarizations is similar to what was seen in Figure 9. Comparing these doses with the higher-energy values at similar angles (~140 mRad vs. ~210 mRad for P-Polarization and ~130 mRad versus ~190 mRad for S-Polarization) shows an approximately linear scaling between incident field energy and dose. These values also compare well to the 3D cylindrical simulations conducted previously [13]. For example, an un-rotated, 50 μm radius gold disk with 75 J field energy incident showed X-ray fluences on-axis near 6-10×10^8 cm^{-3}; this scales to 150-260 mRad dose on-axis, but used an unsophisticated method to scale the number fluence to 1 meter.

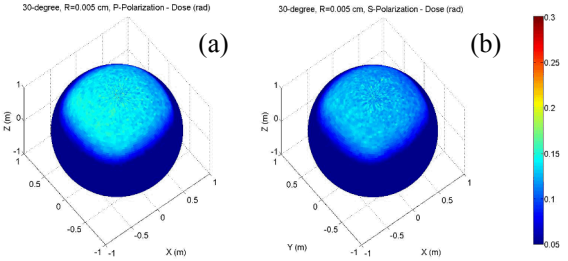

Figure 11. Target doses at 1 meter plotted onto spheres for the lower-energy simulation. Plot (a) is the P-Polarization case, while plot (b) is the same view for the S-Polarization.

Sorting techniques can be used to get energy spectra for certain angle ranges, to look at the difference between the spectra near the disk axis, near the laser axis, and from the disk edge (those X-rays that exit the disk radially). The X-ray macroparticles could be sorted by out-going angle (ϕ for the azimuthal angle and θ for the polar angle) and their angular separation from a given location (ϕ_0, θ_0) calculated. The five angular loci of interest were: (1) the angle $\phi_0 = 0°$, $\theta_0 = 150°$, corresponding to the disk axis on the side facing the laser ("Laser-Side Disk Axis"); (2) $\phi_0 = 180°$, $\theta_0 = 30°$ corresponding to the disk axis on the side facing away from the laser ("Laser-Opposite Disk Axis"); (3) the line θ_0=90°-30°×cos(ϕ_0), which is the angular function for the disk edge and contains X-rays which travel radially through the disk, referred to as "Disk Edge" below; (4) the angle $\phi_0 = 0°$, $\theta_0 = 0°$ corresponding to the positive z-axis and the incident direction of the laser; and (5) the angle $\phi_0 = 0°$, $\theta_0 = 180°$, corresponding to the negative z-axis. These loci are plotted in Figure 1. If a macroparticle had an angle within +/- 5º of any of these locations, it was saved and used in the spectrum calculation, with the results plotted in Figure 12.

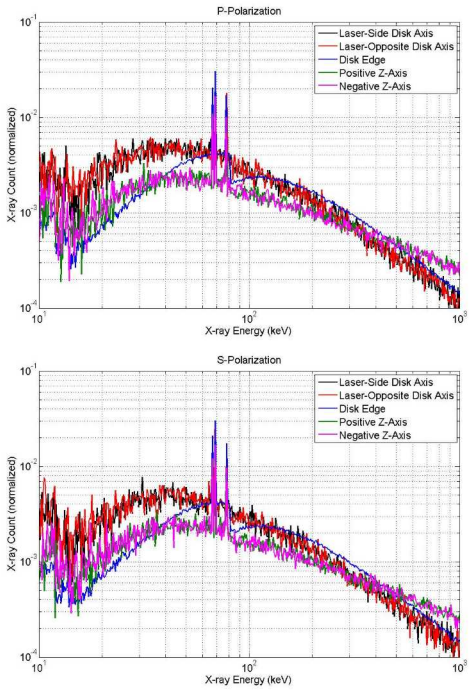

Figure 12. X-ray spectra for the two polarizations looking within +/- 5º of the five loci defined in the text: the disk axis on the side facing away from the incident laser; the disk axis on the side facing the incident laser; the plane of the disk; the positive z-axis; and the negative z-axis.

The "Disk Edge" region had significantly more particles than the other loci, which required the spectra be normalized so a comparison could be made; this also explains the relative smoothness of this curve when compared to the others. The plots indicate that the X-ray spectrum is slightly harder in the "Disk Edge" than at the disk poles, though less hard than along the axis of the laser. The two z-axis curves have a lower level through the spectral lines at 65-80 keV than the curves defined by disk relationships. The dip in the "Disk Edge" spectrum at 80 keV, just after the spectral lines, can be explained by the sudden increase in the total attenuation coefficient for gold at these energies [14]. The X-rays collected for the "Disk Edge" spectrum have to travel through a greater gold thickness, so are affected more by this absorption. Some of the structure in the spectra between 10 and 20 keV can also be explained in this manner.

In order to better aid the Sandia researchers, the 3D Cartesian simulation was modified to use a 100 µm by 100 µm square foil with a 45º tilt. The S-polarized laser pulse had a 500 fs duration, a 5.9 µm FWHM, and a total incident field energy of ~100 J; these are compared to the previous values of 1400 fs, 9.0 µm FWHM, and ~130 J field energy. Because of difficulties with the simulation, time histories for this simulation are only plotted out to 7 ps in Figure 13 -- from previous simulations, in excess of 80% of the X-rays were generated from 0 to 7 ps. The shorter pulse width for the new simulation suggests that a greater proportion of the X-rays will be produced by 7 ps, so a scaling up of the dose by 20-25% should account for the shorter dose integration time. The peak number of X-rays was lower than the previous simulations, but the peak X-ray energy had a higher value as did the average energy per X-ray. The electron energy was slightly lower, due to the shorter pulse width.

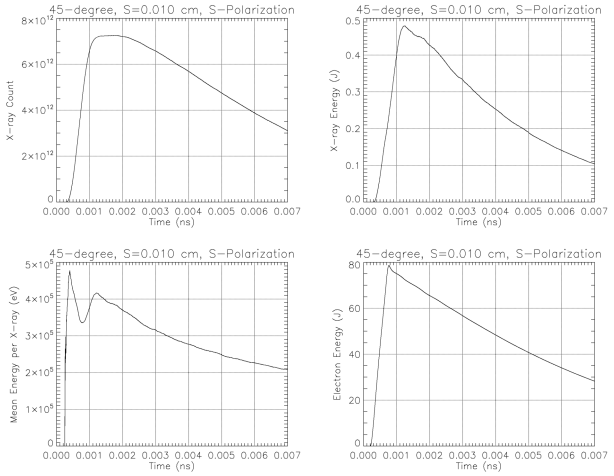

Figure 13. Time histories of global X-ray count, total X-ray energy, and energy per X-ray for 3D Cartesian S-Polarization simulation with a 100 µm square foil tilted by 45º.

The X-ray spectrum showed the same shape as in Figure 9, though with monotonically lower values due to the lower number of X-rays generated. Averaging the total X-ray production over a 1 meter sphere and scaling from fluence to dose, the X-ray production of 7.17×10^{13} results in 148.3 mRad over 7 ps. A quick scaling by 20% to extrapolate to 10 ps gives 8.60×10^{13} total X-rays and 178.0 mRad, averaged; this 10 ps dose value is higher than from the previous S-Polarization simulation. The scaled 1 meter dose is plotted in Figure 14 and shows values from 220 mRad (near the disk axes) to 140 mRad (near the disk edge). This lower value matches with experimentally measured values on the foil edge that were on the order of 100 mRad.

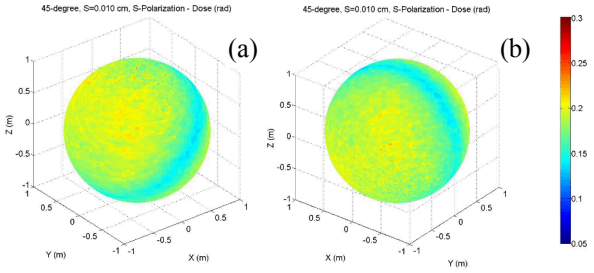

Figure 14. Target doses at 1 meter plotted onto spheres. Plots (a) and (b) are two views from opposite sides of the sphere for the integrated dose scaled up by 20% to estimate the dose at 10 ps.

VI. SUMMARY AND CONCLUSION

LSP was used to create 3D cylindrical and Cartesian simulations of a dynamic IR laser / high-atomic-number foil interaction for use as a bremsstrahlung X-ray source.

The 3D cylindrical simulations showed the dose had a strong dependence on foil radius, though the exact levels produced were hard to evaluate due to signal noise from the low numbers of X-ray macroparticles produced, especially near the z-axis. This trend was very useful when going forward to the Cartesian simulations, which maintained the 50 μm foil radius. The 3D Cartesian simulations showed the greatest utility for dose calculations, energy conservation, and maintaining the full physics of the laser / plasma interaction. This came at a cost, however, as these calculations were the most computationally intensive. However, the interaction was found to have dynamic features that could not be fully represented except in 3D Cartesian. The typical 1 meter dose was in the 150-250 mRad range, showing a nearly factor of 2 variation with angle. For the 100 μm square foil tilted at 45º, the simulated dose at 1 meter varied from 140-210 mRad, comparable to the experimental value of ~100 mRad. Interestingly, a higher-intensity laser pulse produced a higher dose, even though the pulse-length was shorter for lower total incident field energy. Future work will examine the sensitivity of the spectrum to the characteristic length of the blow-off plasma and determine the best method to mitigate its effect on the radiograph.

VII. REFERENCES

[1] R. B. Campbell and B. V. Oliver, LDRD proposal (2009).

[2] P. Rambo, J. Schwarz, M. Geissel, E. Brambrink, A. Edens, M. Kimmel, and B. Atherton, "The Z-Petawatt Laser at Sandia National Laboratories," in Conference on Lasers and Electro-Optics/Quantum Electronics and Laser Science Conference and Photonic Applications Systems Technologies, OSA Technical Digest (CD), paper JTuA50 (2008).

[3] L. E. Ruggles, J. L. Porter, P. K. Rambo, W. W. Simpson, M. F. Vargas, G. R. Bennett, and I. C. Smith, "Measurements of 4–10 keV x-ray production with the Z-Beamlet laser," Rev. Sci. Instrum. 74, 2206 (2003).

[4] G. R. Bennett, O. L. Landen, R. F. Adams, J. L. Porter, L. E. Ruggles, W. W. Simpson, and C. Wakefield, "X-ray imaging techniques on Z using the Z-Beamlet laser," Rev. Sci. Instrum. 72, 657 (2001).

[5] R. D. Edwards, M. A. Sinclair, T. J. Goldsack, et al., "Characterization of a gamma-ray source based on a laser-plasma accelerator with applications to radiography," Appl. Phys. Lett. 80, 2129 (2002).

[6] J. Galy, M. Maučec, D. J. Hamilton, R. Edwards, and J. Magill, "Bremsstrahlung production with high-intensity laser matter interactions and applications," New J. Phys. 9, 23 (2007).

[7] D. R. Welch, D. V. Rose, M. E. Cuneo, R. B. Campbell, and T. A. Mehlorn, "Integrated simulation of the generation and transport of proton beams from laser-target interaction," Phys. Plasmas 13, 063105 (2006).

[8] C. Thoma, R. E. Clark, T. C. Genoni, and B. V. Oliver, "LSP simulations of laser plasma interactions for applications to laser-driven radiography," Mission Research Report No. MRC/ABQ-R-2092 (2003).

[9] D. R. Welch D. R. Welch, D.V. Rose, R. E. Clark, C. B. Mostrom, W. A. Stygar, and R. J. Leeper, "Fully kinetic particle-in-cell simulations of a deuterium gas puff z pinch," Phys. Rev. Lett. 103, 255002 (2009).

[10] S. Balay, W. D. Gropp, L. C. McInnes, and B. F. Smith, "Efficient Management of Parallelism in Object Oriented Numerical Software Libraries," in Modern Software Tools in Scientific Computing, edited by E. Arge, A. M. Bruaset, and H. P. Langtangen, pp. 163-202. Birkhäuser Press (1997).

[11] J. A. Halbleib, R. P. Kensek, G. D. Valdez, S. M. Seltzer, and M. J. Berger, "ITS: The Integrated TIGER Series of electron/photon transport codes - version 3.0," IEEE Trans. Nucl. Sci. NS-39, 1025 (1992).

[12] D. V. Rose, D. R. Welch, et al., "Coupled particle-in-cell and Monte Carlo transport modeling of intense radiographic sources," J. Appl. Phys. 91, 3328 (2002).

[13] D. R. Welch, C. L. Miller, R. B. Campbell, and B. V. Oliver, "Laser radiography," Voss Scientific Report VSL-0914 (2009).

[14] M. J. Berger, J. H. Hubbell, S. M. Seltzer, J. Chang, J. S. Coursey, R. Sukumar, and D. S. Zucker, "XCOM: Photon Cross Sections Database," http://www.nist.gov/physlab/data/xcom/index.cfm (retrieved 22 September 2010).